Ionization and neutral gas heating efficiency in radio frequency electrothermal microthrusters: The role of driving frequency

Sid Leigh (ID) ; Scott J. Doyle (ID) ; Gregory J. Smith (ID) ; Andrew R. Gibson (ID) ; Rod W. Boswell (ID) ;
Christine Charles (ID) ; James P. Dedrick ✉ (ID)

Check for updates

View Online

Export Citation

Ionization and neutral gas heating efficiency in radio frequency electrothermal microthrusters: The role of driving frequency

View Online   Export Citation   CrossMark

Sid Leigh,[1] [iD] Scott J. Doyle,[2] [iD] Gregory J. Smith,[3] [iD] Andrew R. Gibson,[4] [iD] Rod W. Boswell,[5] [iD]
Christine Charles,[5] [iD] and James P. Dedrick[1,a) [iD]

AFFILIATIONS

[1]York Plasma Institute, School of Physics, Engineering and Technology, University of York, Heslington, York YO10 5DD, United Kingdom
[2]Electrical Engineering and Computer Science, University of Michigan, 1301 Beal Ave., Ann Arbor, Michigan 48109-2122, USA
[3]Research group PLASMANT, Department of Chemistry, University of Antwerp, Universiteitsplein 1, BE-2610 Antwerp, Belgium
[4]Research Group for Biomedical Plasma Technology, Ruhr-Universität Bochum, Universitätstraße 150, 44801 Bochum, Germany
[5]Space Plasma, Power and Propulsion Laboratory, Research School of Physics, The Australian National University, Canberra, ACT 2601, Australia

a)Author to whom correspondence should be addressed: james.dedrick@york.ac.uk

ABSTRACT

The development of compact, low power, charge–neutral propulsion sources is of significant recent interest due to the rising application of micro-scale satellite platforms. Among such sources, radio frequency (rf) electrothermal microthrusters present an attractive option due to their scalability, reliability, and tunable control of power coupling to the propellant. For micropropulsion applications, where available power is limited, it is of particular importance to understand how electrical power can be transferred to the propellant efficiently, a process that is underpinned by the plasma sheath dynamics. In this work, two-dimensional fluid/Monte Carlo simulations are employed to investigate the effects of applied voltage frequency on the electron, ion, and neutral heating in an rf capacitively coupled plasma microthruster operating in argon. Variations in the electron and argon ion densities and power deposition, and their consequent effect on neutral-gas heating, are investigated with relation to the phase-averaged and phase-resolved sheath dynamics for rf voltage frequencies of 6–108 MHz at 450 V. Driving voltage frequencies above 40.68 MHz exhibit enhanced volumetric ionization from bulk electrons at the expense of the ion heating efficiency. Lower driving voltage frequencies below 13.56 MHz exhibit more efficient ionization due to secondary electrons and an increasing fraction of rf power deposition into ions. Thermal efficiencies are improved by a factor of 2.5 at 6 MHz as compared to the more traditional 13.56 MHz, indicating a favorable operating regime for low power satellite applications.

I. INTRODUCTION

Prospective applications of low mass, low cost satellite platforms such as the CubeSat[1] have led to the development of miniaturized propulsion systems, enabling small satellites to perform altitude control, drag recovery, and formation flying.[2–4] The challenging design requirements of microthrusters, which require robust, compact, and power-efficient designs,[5–7] have meant their implementation so far has been limited.[8–10] Modeling of such sources aids in optimization of their design and operational regime; many such models exist for micro plasma sources.[11–13] Radio-frequency (rf) electrothermal microthrusters use an rf plasma discharge to heat gaseous propellant, enabling the deposition of power to be spatially and temporally controlled.[14–17] One such source is the *Pocket Rocket*, which operates via capacitive coupling at low powers (up to 50 W) neutralizer-free plasma microthruster.[18–20] *Pocket Rocket* operates in argon and xenon at pressures above ∼133 Pa (1 Torr),[21,22] heating propellant gas to temperatures of ∼1000 K, and generating thrust to the order of 1 mN.[23,24] Continued development of the *Pocket Rocket* and similar micropropulsion sources requires that the neutral heating mechanisms and power coupling efficiency are optimized without compromising on the physical size.

The growing commercial availability of rf power delivery systems operating below 13.56 MHz potentially offers low-frequency alternatives to existing micropropulsion systems. Such low-frequency sources have been explored in previous work in Refs. 20 and 25, and by others developing rf electrothermal thrusters in Refs. 26 and 27, indicating growing interest in this area.

During operation of the *Pocket Rocket*, a dc self-bias voltage forms on the dielectric radial wall between the powered electrode and the plasma.[13,28] The dc self-bias voltage arises to balance the net plasma current density at the powered and grounded electrodes, the latter of which being significantly larger in surface area.[29] Ions are radially accelerated through the sheath toward the dielectric wall, heating gas via ion–neutral charge exchange collisions.[30] This process leads to gas heating on the relatively short (submillisecond) timescales taken for breakdown to occur and for the plasma to stabilize.[21] Compared to the timescales for charge exchange gas heating, the heating of the radial wall by ion bombardment provides conductive gas heating over longer timescales of 10–100 s.[21] Ion bombardment induces the emission of secondary electrons via the Auger process,[31] which are accelerated through the sheath potential into the plasma bulk at over 50 eV.[32,33] Secondary electrons generally have a beam-like energy distribution with significantly higher mean energies than bulk electrons, and hence represent an efficient mechanism for further ionization and gas heating.[34–36]

Alongside ion–neutral charge exchange, several spatiotemporally complex electron heating mechanisms are also exhibited within the rf discharge, each dependent upon applied voltage frequency, voltage amplitude, pressure, and geometry.[19,37] At low voltages (typically less than 300 V at 1 Torr), α-mode heating represents the predominant electron acceleration mechanism. Here, bulk electrons are accelerated through electric fields arising via the periodic collapse and expansion of plasma sheaths.[38–40] At higher applied voltages (larger than 300 V at 1 Torr), the *Pocket Rocket* switches into γ-mode operation, with the discharge being sustained primarily through secondary electron impact ionization.[24,41] This transition introduces a degree of non-linearity to the system, as the flux of secondary electrons is proportional to the ion flux incident upon material surfaces, which is itself proportional to the secondary electron ionization rate. Furthermore, secondary ionization events are observed over a wider volume than α-mode bulk ionization events, occurring in both the sheath and within the bulk, arising due to the secondary electron mean-free-path being comparable to the source diameter.[42] In particular, secondary electrons are predominantly oriented toward the central axis due to the cylindrically symmetric hollow cathode geometry.[32] The enhanced spatial control afforded through carefully structured electrode geometries is, in-fact, the topic of some considerable interest within the areas of materials processing and space propulsion.[43–46] Capacitively coupled argon plasmas have been studied at a range of pressures from a few mTorr[47,48] to tens-hundreds Torr.[49] These studies have investigated the effect of changing voltage frequency on α- and γ-mode operation, at frequencies below 13.56 MHz (Refs. 50 and 51) and above 13.56 MHz.[52,53] In this work, the electron and ion heating mechanisms in a hollow cathode geometry are presented for driving voltage frequencies below 13.56 MHz, extending the spatiotemporal analysis beyond the range previously studied by Doyle *et al.*,[19,54] Ho *et al.*,[55] and Grieg[56] detailing a neutral gas heating optimized frequency regime in the *Pocket Rocket* microthruster.

In this work, two-dimensional (2D) fluid-kinetic simulations were performed to investigate variations in electron, ion, and gas

heating at applied voltage frequencies ranging from 6 to 108 MHz at 450 V. Descriptions of the *Pocket Rocket* source, numerical methods, and diagnostic procedures are given in Sec. II. In Sec. III A, spatial distributions of macroscopic plasma parameters are presented to describe how the processes of neutral heating and ionization are connected. These include neutral gas density and temperature, Ar^+ ion density, dc self-bias wall potential, and secondary electron ionization rates. Phase-resolved electron ionization dynamics are investigated with applied voltage frequency in Sec. III C. Section IV A describes the effect of voltage frequency on the dc self-bias voltage and the subsequent impact on the argon ion flux and neutral gas temperature. Finally, the effect of voltage frequency on spatial rf power deposition and the fraction of power deposited into ions are presented in Sec. IV B.

II. SIMULATION MODEL AND NUMERICAL METHODS

Two-dimensional fluid-kinetic simulations of the *Pocket Rocket* microthruster source were performed using the Hybrid Plasma Equipment Model (HPEM).[57] The simulation geometry is shown in Fig. 1. Complete descriptions of the source and numerical methods used are given in Refs. 19 and 57, respectively, and a summary is given here. HPEM has previously been extensively corroborated with phase-resolved optical emission spectroscopy (PROES) measurements in the *Pocket Rocket* microthruster operated using single frequency (13.56 MHz) waveforms at varying applied voltage,[19] varying the frequency (13.56–40.68 MHz) at constant voltage,[42] dual-frequency waveforms,[58] and multi-harmonic tailored waveforms.[54] Throughout these previous studies, a good agreement between the electron dynamics inferred from PROES measurements via the excitation of the Ar ($2p_1$) state and those simulated using HPEM has been obtained.

The source consists of a dielectric alumina tube (18 mm length, 4.2 mm inner diameter), a 5 mm long rf-powered annular electrode centered at an axial distance of $Z = 21$ mm from the plenum edge, and two grounded electrodes at either side of the rf electrode. Argon gas is introduced to the plenum cavity at 100 sccm (2.98 mg s^{-1}) via a 3 mm diameter inlet, centered at $Z = 6$ mm. The gas flows through the source in the $+Z$ direction toward the expansion region. Gas is extracted at the far end of the expansion region ($Z = 73$ mm), where a fixed
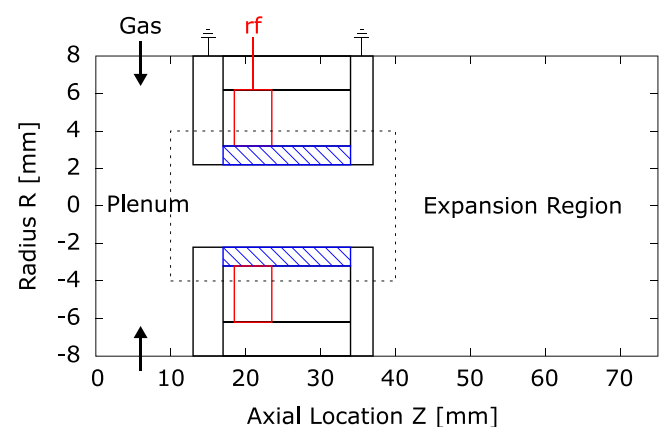

FIG. 1. Diagram of the simulation domain, axisymmetric about $R = 0$ mm (not to scale). Outlined are the grounded electrodes (black), rf-powered electrode, dielectric radial wall (blue hatched), gas inlet (black arrows), and the region of interest (dashed rectangle).

pressure boundary condition is maintained at 113 Pa (0.85 Torr), matching experimental conditions.[19,42] Pressure is equilibrated between the inlet flow rate and this downstream pressure boundary, maintaining a pressure of between 186 and 226 Pa (1.4–1.8 Torr) within the source discharge region.

The simulation domain is a cylindrical 2D-axisymmetric mesh of 64×152 ($R \times Z$) rectilinear cells, where R and Z are the radial and axial distances, respectively. This provides a radial resolution of 0.125 mm/cell and an axial resolution 0.5 mm/cell. Here, the finer radial resolution is required to resolve the radial electric field gradient through the powered electrode sheaths, such that the sheath extent and velocity can be determined. The radial extent of the sheath edge S_R is calculated as in Ref. 58, where S_R is defined as the radius R that satisfies the Brinkmann criterion.[59] The Brinkmann sheath criterion defines the sheath edge as the radius at which the electron density integrated from the wall is equal to the effective positive charge density minus the electron density integrated from the most positive plasma potential.

A hybrid fluid/kinetic approach was employed in this work. Bulk neutral and ion densities, fluxes, and temperatures were obtained from mass, momentum, and energy continuity equations, while the bulk electron flux is obtained via Scharfetter–Gummel drift–diffusion approximation.[60] The mass continuity boundaries are set to zero for all materials except for the inlet and outlet, where a positive or negative mass flux across the plasma-inlet is allowed. The momentum continuity equation is bounded in a similar fashion, where momentum between cells is conserved at all metal and dielectric boundaries, but is allowed to vary across the inlet and outlet boundaries. The energy continuity equation is bounded by a fixed outer mesh boundary temperature of 325 K, and on the inlet and outlet surfaces. Volume and surface potentials were then obtained from charged species densities employing a semi-implicit solution to Poisson's equation, as described in Ref. 57. Boundary conditions for Poisson's equation were defined by applying a time-dependent RF voltage $\phi_{rf}(t)$ to the powered electrode surface, and zero voltage to both the grounded electrode surfaces and the outer boundary of the mesh, for numerical stability. Here, $\phi(t) = \phi_{rf} \sin(2\pi\nu_{rf}t)$, where ν_{rf} is the frequency, and ϕ_{rf} is the applied voltage amplitude. Power deposition is computed for each charged species as the multiple of the charged particle current and the electric field. Energy distribution functions for bulk ions and neutrals were assumed to be Maxwellian, due to the relatively high operating pressure of ~ 1 Torr. Bulk electron energy distributions in each cell were obtained from the solution of the two-term approximation of the Boltzmann equation and employed to determine the electron temperature and electron impact ionization rates. Secondary electron energy distributions were obtained and tracked via Monte Carlo algorithm, statistically generating solutions to the Boltzmann equation.[61] Here, secondary electrons were emitted from surfaces in proportion to the incident ion flux, mediated by an energy-independent emission coefficient γ.[61,62] Here, the secondary electron emission coefficient is set to $\gamma = 0.2$ for the alumina surface and $\gamma = 0.0$ for all other surfaces. Secondary electrons are released with an initial energy of 3 eV and subsequently accelerated through the sheath to non-thermal energies. Omission of secondary electron emission from other surfaces was undertaken to reduce computational expense as the secondary electron yield emitted from other surfaces was negligible compared to that of the alumina surface due to the lower ion fluxes and sheath voltages at

the grounded surfaces in the studied plasma system in comparison to the alumina surface.

Species considered within the model included: Ar, Ar(4s), Ar(4p), Ar(4d), Ar_2^*, Ar^+, Ar_2^+, and e^- employing the reaction mechanism as described in Ref. 63. Here, Ar(4p) and Ar(4d) are lumped excited states, where Ar(4p) consists of Ar(4p, 3d, 5s, and 5p), while Ar(4d) contains Ar(4d), Ar(6s), and Rydberg states. As noted above, two electron species were tracked, bulk electrons produced via ionisations in the gas phase, and secondary electrons released from material surfaces. Gas-phase electron–neutral and electron–ion collisions included elastic, excitation, and ionization reactions where the rate coefficients were specified in Arrhenius form.[57] Heavy particle interactions included: cascade processes, multistep ionization, and heavy particle mixing between excited species using interaction cross sections obtained from Refs. 64–67. Ion–neutral charge exchange collisions were employed with a rate coefficient of 5.66×10^{-10} cm^{-3} ($T_g/300$)$^{0.5}$, where T_g is the neutral gas temperature.[68] Heat exchange between the gas and the wall is handled via a conduction model.[57,69] Power to material surfaces is calculated from the thermal gradient between the gas and the wall and the kinetic energy delivered by ion fluxes incident upon plasma facing surfaces. Heat transferred to the wall is removed from the gas as a negative enthalpy term in the energy conservation equation. Material thermal conductivities K_T were specified as follows: for metals: $K_T = 1$ W cm^{-1} K^{-1}, for alumina: $K_T = 0.15$ W cm^{-1} K^{-1}, and for macor: $K_T = 0.018$ W cm^{-1} K^{-1}. A thermal energy accommodation coefficient of 0.4 was also applied to plasma-facing materials, as discussed in Ref. 19. The outer boundary of the mesh was maintained at 325 K.

Simulations were undertaken at applied voltage frequencies ν_{rf} between 6 and 108 MHz at a fixed voltage amplitude of $\phi_{rf} = 450$ V (900 V peak-to-peak). Such conditions enabled a comparison of the ionization dynamics within a γ-mode discharge, negating mode transition effects.[19] A lower limit of 6 MHz was imposed so as to remain within the ion-matrix regime, where the ion-plasma frequency ω_{pi} is significantly below the RF driving frequency ν_{rf}, and hence, ion mobility is dictated primarily by time-averaged DC fields. One computational iteration ranged from 8.33 μs at 6 MHz, to 0.461 μs at 108.48 MHz, maintaining a temporal resolution of 5 rf cycles. At convergence, the phase-resolved motion was captured employing significantly higher temporal resolutions, maintaining a 2° resolution, i.e., 180 points per RF phase cycle. Data from these final iterations are presented in Sec. III C.

As described above, the distribution of electrostatic fields in the plasma is calculated by the solution of the Poisson equation. While this is expected to be an appropriate model under a wide range of conditions, plasma sources operated at high driving frequencies and electron densities can exhibit complex electromagnetic phenomena that cannot be captured using this approach. A review of such effects in the context of large area capacitively coupled plasmas (CCPs), where they have been studied extensively, is given in Ref. 70. Two of the main effects are related to the formation of standing waves, and the skin effect.

Standing wave effects occur when the wavelength of the driving frequency, which is reduced in the presence of the plasma, approaches the length scales of the electrode system. In large area CCPs, this is typically the electrode radius, which can be in the range of tens of cm. For 108.48 MHz, the highest frequency considered in this work, the free

08 May 2024 08:45:18

space wavelength is approximately 2.7 m. An indication of the reduction of the wavelength in the presence of the plasma can be obtained from the formulas presented in Refs. 47 and 48. It should be noted that these formulas are derived in the context of conventional CCP systems, where the geometric arrangement is different to that used here, and the electromagnetic phenomena will differ in the specific details. As a result, they are used only here to provide an indication of the potential importance of such effects. Using typical plasma parameters predicted by the simulations carried out here leads to a reduced wavelength in the range of 1.5–2 m, which is significantly larger than the dimensions of the Pocket Rocket source. As a result, significant standing wave effects appear unlikely.

Skin effects in CCP systems can become relevant when the electron density is large enough to lead to a skin depth smaller than the characteristic dimensions of the plasma.[70] Here, the skin depth can be calculated by taking typical electron densities/temperatures and neutral gas densities from the simulations presented later in the results sections, and using the expression for the skin depth given in Ref. 71. Over the range of driving frequencies considered in this work, the skin depth is larger than the dielectric tube diameter at lower frequencies and decreases with increasing frequency such that it is similar to, or less than, the diameter of the dielectric tube at the higher frequencies studied. Because of this, skin effects may play a more important role as the frequency is increased. While the overall importance of such effects is difficult to assess within the frame of this work, they are not anticipated to change the overall trends presented in the results section. Nevertheless, the potential that such effects may be present in reality and not captured in the current model should be kept in mind when interpreting the results presented.

III. THERMAL RAREFACTION AND SPATIO-TEMPORAL IONIZATION RATES

### A. Macroscopic plasma properties at 10 MHz

The neutral gas density, neutral gas temperature, and argon ion density within the source region are shown in Figs. 2(a)–2(c), respectively, for operation at 10 MHz, 450 V, with 100 sccm of argon. Axially resolved 1D profiles of the dc self-bias voltage η_{dc}, bulk ι_α, and secondary ι_γ ionization rates are presented in Fig. 2(d). The dashed lines indicate two axial locations of interest: (1) $Z = 18.6$ mm, the region of highest ion density, and (2) $Z = 22.0$ mm, the axial midpoint of the powered electrode. As described in Ref. 19 in the geometrical arrangement of the Pocket Rocket, the powered electrode is separated from the plasma by the alumina dielectric. This leads to the build up of a negative surface charge on the dielectric which functions similarly to the dc self-bias in a conventional capacitively coupled plasma with an exposed metal electrode and a blocking capacitor installed in the external circuit. In this context, when we refer to the dc self-bias voltage η_{dc}, we are referring to the net negative surface charge on the dielectric.

A localized rarefaction in the neutral argon density occurs downstream of location 2 in Fig. 2(a), arising from the increased neutral gas heating presented in Fig. 2(b). From locations 1 to 2, the on-axis $(R = 0$ mm$)$ n_{Ar} decreases by half from 2.80×10^{22} to 1.43×10^{22} m^{-3}. Across the same range in Fig. 2(b), the on-axis neutral gas temperature T_g correspondingly increases by 75% from 511 to 895 K. Further downstream, heat and ion losses to the dielectric walls (initialized at 325 K) leads to a decreasing gas temperature T_g toward the outlet, while n_{Ar} gradually recovers.

In Fig. 2(c), the Ar$^+$ ion density n_{Ar^+} has a highly localized maximum on-axis just upstream of the powered electrode at location 1, at 2.60×10^{18} m^{-3}. This coincides with where T_g is slightly lower and n_{Ar} is higher than near the walls or further downstream. From location 1 to 2, the on-axis n_{Ar^+} decreases by 55% to 1.15×10^{18} m^{-3}, similar to the decrease observed in n_{Ar}. Thus, the reduction in both n_{Ar^+} and n_{Ar} can both be attributed to thermally driven rarefaction, directly as a result of heating via collisional charge exchange in which both species are thermally coupled. Despite the localized decrease in n_{Ar} at location 2, the axial pressure gradient exhibits a smooth axial profile, ranging from 1.7 Torr in the plenum to 0.8 Torr downstream of the aperture at $Z = 38$ mm. The pressure gradient is maintained against the temperature-driven rarefaction of the gas, and since the increase in T_g offsets the decreased n_{Ar} through the ideal gas law, this indicates that neutral depletion through ionization—while present—is not a significant factor in the reduction of n_{Ar} near location 2. This is supported by the fact that from locations 1 to 2, n_{Ar^+} experiences a greater decrease than n_{Ar}.

The axial profile of the dc self-bias voltage η_{dc} at the radial wall $(R = 2.1$ mm$)$ is shown by the black curve in Fig. 2(d). From locations 1 to 2, η_{dc} doubles from -145 to -272 V, its most negative value, coinciding with the axial midpoint of the rf powered electrode as expected. It is within reason that the stronger η_{dc} at location 2 would attract higher fluxes of ion losses to the walls, contributing to the reduction of n_{Ar^+} here. This is further discussed in Sec. IV A, where agreement is seen between a more negative η_{dc} and a higher radial Ar$^+$ flux. Note that the 10 MHz rf sheath potential, while present, is not expected to affect the motion of the ions. Note also, the substantial overlap between the axial region of highest on-axis Ar$^+$ density in Fig. 2(c) and the most negative dc self-bias voltage in Fig. 2(d). This overlap enforces a significant radial ion flux, accelerated radially through the ≈ 240 V dc sheath potential, that is an order of magnitude higher than the axial ion flux, accelerated axially through the ≈ 60 V quasi-dc plasma potential.[19] This enhanced radial ion flux is indirectly responsible for the high secondary electron impact ionization rate, relative to bulk (rf-driven electron) impact ionization rates.

Figure 2(d) also shows the on-axis phase-averaged ionization rates by secondary electrons ι_γ (red) and bulk electrons ι_α (blue). In general, ι_γ exceeds ι_α across most of the thruster axis to approximately $Z = 32$ mm, thus exhibiting a predominantly γ-mode discharge under these conditions (see Sec. III C). From locations 1 to 2, ι_α almost doubles from 3.47×10^{23} to 6.66×10^{23} m^{-3} s^{-1}. Over this range, ι_γ reduces by 30% from 3.81×10^{24} to 2.63×10^{24} m^{-3} s^{-1}, corresponding to being a factor 11 higher than ι_α to just over a factor of 4 higher. The profile of ι_γ closely follows that of n_{Ar^+} in Fig. 2(c), which are both preferentially weighted upstream with maxima at location 1 and tails extending downstream. With secondaries accounting for the majority of the ionization in the γ-mode discharge, the 30% reduction in ι_γ between locations 1 and 2 is in agreement with the 55% reduction in n_{Ar^+}. This is despite the dc self-bias η_{dc} being twice the magnitude at location 2, which would contribute to ι_γ by attracting a greater flux of ions to the wall to release more secondary electrons. Instead, ι_γ is more sensitive to the neutral density as influenced by the temperature T_g that results from ion–neutral collisions, as indicated by the maximum at location 1, where T_g is 75% lower and neutral gas is twice the density, and the probability of electron–neutral impacts is higher. However, ι_γ is ultimately dependent on the dc self-bias potential η_{dc}
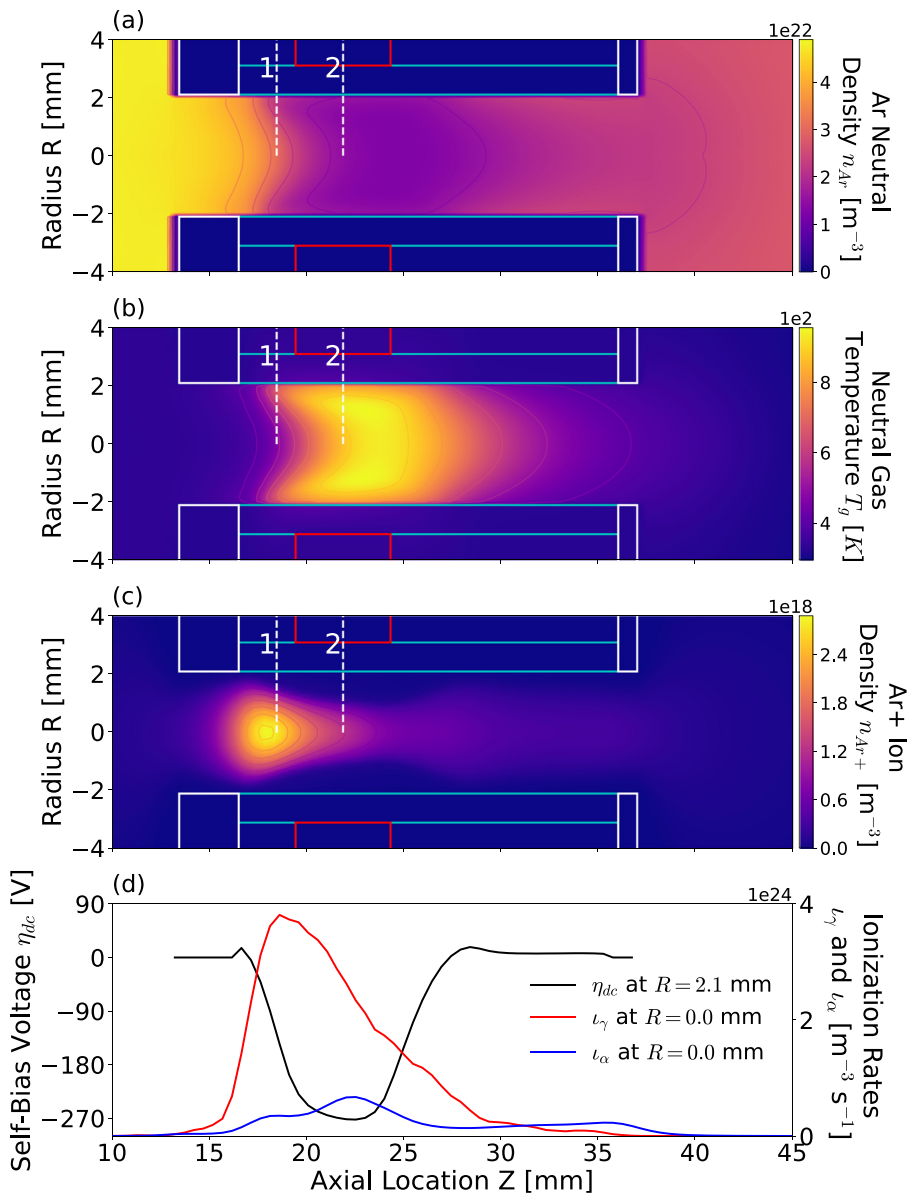
FIG. 2. Phase-averaged, spatially resolved (a) neutral argon gas density n_{Ar} (b) neutral gas temperature T_g, (c) Ar^+ ion density n_{Ar^+}, and (d) 1D axial profiles of (i) dc self-bias potential η_{dc} at the radial wall ($R = 2.1$ mm, 13 mm $\leq Z \leq 37$ mm), (ii) on-axis ($R = 0$ mm) secondary electron ionization rate ι_γ, and (iii) on-axis bulk electron ionization rate. Applied voltage $\phi_{rf} = 450$ V at 10.0 MHz, employing 100 sccm argon, wall temperature 325 K. Outlined are the grounded electrodes (white), rf-powered electrode (red), and dielectric radial wall (cyan). Two Z locations of interest "1" (18.6 mm) and "2" (22.0 mm) shown by dashed lines.

that provides the wall-bound ion flux. As η_{dc} reduces rapidly upstream of location 1 and downstream of 2, ι_γ correspondingly declines, though is still finite even where η_{dc} is zero or positive due to the axial motion of the electrons. Hence, the peak of ι_γ at location 1 hence represents an optimum trade-off between these two mechanisms of neutral heating and secondary electron production for the conditions employed here.

By contrast, for bulk electrons, ι_α is a maximum at location 2, marking the center of the rf electrode that provides the sheath potential and η_{dc}, the latter being most negative at this axial location. Across the axial length of the dielectric alumina tube (18 mm $\leq Z \leq 36$ mm) where the sheath potential is sustained, ι_α remains relatively level even in regions of near-zero η_{dc}, contributing to the downstream tail of n_{Ar^+} in Fig. 2(c) as ι_γ declines. At the grounded electrodes beyond either

end of the dielectric, ι_α rapidly declines as the sheath potential drops to zero. Compared with ι_γ, the optimum trade-off for ι_α is instead weighted toward the strength of these potentials, particularly the sheath potential, rather than the neutral density and temperature. The difference in the main limiting factors between bulk and secondary electron ionization lies in the processes by which each receive energy. Bulk electrons are dependent on the oscillation of the sheath potential that expands and contracts into the plasma bulk. As distinct from this, secondary electrons are initially emitted at the wall with initial energies of 3 eV, then immediately gain more from the dc self-bias and sheath potentials there. Quantification of the gas-phase electron and ion energy distributions is out of the scope of this work. However, the explanation provided above is supported by the observation that ι_γ

were more influenced by changes in n_{Ar} and T_g, and less so by ι_α that was more closely linked with variations in rf electrode potential.

Therefore, within the complex interplay of the plasma parameters in Fig. 2, there is a balance between the heating of the gas by ion–neutral charge exchange collisions and the associated electron-driven ionization processes. All of these are influenced by the applied voltage frequency, which is investigated in detail below.

B. Macroscopic plasma parameters with varying single driving frequency

To investigate the effects of voltage frequency on ionization, the on-axis ($R = 0$ cm) neutral argon and Ar^+ density profiles are shown with respect to applied voltage frequency in Figs. 3(a) and 3(b) over the range 6–108 MHz. All discharges employ the same conditions as shown previously, $\phi_{rf} = 450$ V with 100 sccm of argon.

The neutral argon density in Fig. 3(a) is highest in the plenum region ($Z \leq 13$ mm) and lowest in the vicinity of the powered electrode ($15 \leq Z \leq 27$ mm) for all applied voltage frequencies, agreeing with the distribution shown previously in Fig. 2(a). As before, the reduction in neutral density n_{Ar} is attributed to thermally induced rarefaction through ion–neutral charge collisions, where ions are accelerated by the dc self-bias potential.[19] Increasing the applied voltage frequency for a fixed voltage amplitude results in enhanced neutral heating and reduced neutral densities at the powered electrode ($Z = 21$ mm). Here, the neutral density n_{Ar} decreases by a factor of 2.5, from 2×10^{22} at 6 MHz to 8×10^{21} m^{-3} at 108 MHz.

Figure 3(b) shows that the Ar^+ density reaches a maximum upstream of the powered electrode, peaking in the region of $Z = 15$–20 mm for all applied voltage frequencies. Although the change the ion density distribution is gradual, three broad regions exhibiting differing behavior can be identified. First, from 6 to 13.56 MHz, the maximum on-axis ion density increases by a factor of 1.4, from 1.8×10^{18} to 2.5×10^{18} m^{-3}. Second, from 13.56 to 40.68 MHz, the maximum on-axis ion density reduces slightly to 2.3×10^{18} m^{-3} at 27.12 MHz, before increasing back to 2.5×10^{18} m^{-3} at 40.68 MHz.

It should be noted that the overall rate of ionization continues to increase over this voltage frequency range (see Fig. 4 and Sec. III C). Third, in the range 40.68–108.48 MHz, the maximum on-axis argon ion density increases by 40%, up to 3.6×10^{18} m^{-3}. The complex dependency of the ion density as a function of voltage frequency results from the variation in the production and loss processes of the ions, which both depend on the neutral Ar density [see Fig. 2(a)]. The observation that similar mamixa in the on-axis ion density are observed at 13.56 and 40.68 MHz, suggests that a comparable degree of ion–neutral gas heating could be achieved at the lower frequency of 13.56 MHz using a fraction of the input power.

Thermal rarefaction at the powered electrode ($15 \leq Z \leq 27$ mm in Fig. 1) also slightly shifts the location of maximum argon ion density upstream by approximately 2 mm, from $Z = 19$ mm at 6 MHz, to $Z = 17$ mm at 108.48 MHz. Over this range, the argon ion density distribution also becomes less localized to the powered electrode, with the on-axis argon ion density increasing significantly by a factor of 25 at the inlet ($Z = 10$ mm) and by a factor of five at the outlet ($Z = 38$ mm). These contributions arise from enhanced α-mode ionization mechanisms during sheath collapse and sheath expansion that occur along the full length of the thruster, and will be discussed in more detail in Sec. III C. However, in general, the maximum argon ion density remains upstream of the powered electrode throughout the range 6–108 MHz. It will now be shown that γ-mode ionization via secondary electrons constitutes the dominant ionization mechanism.

The phase-averaged on-axis ($R = 0$ cm) secondary electron ionization rate for voltage frequencies in the range 6.0–108.48 MHz at 450 V is shown in sigure 4.

In Figs. 4(a) and 4(b), respectively, the bulk and secondary ionization rates both reach a maximum near the upstream edge of the powered electrode ($Z = 17.5$ and $Z = 18.6$ mm) throughout the voltage frequency range of 6–108 MHz. More generally, significant secondary electron ionization can be observed to occur along the axial length of the dielectric wall ($17 \leq Z \leq 34$ mm), coinciding with the axial extent of the dc self-bias voltage, shown previously in Fig. 2, where secondaries are released at a rate proportional to the radial ion flux incident
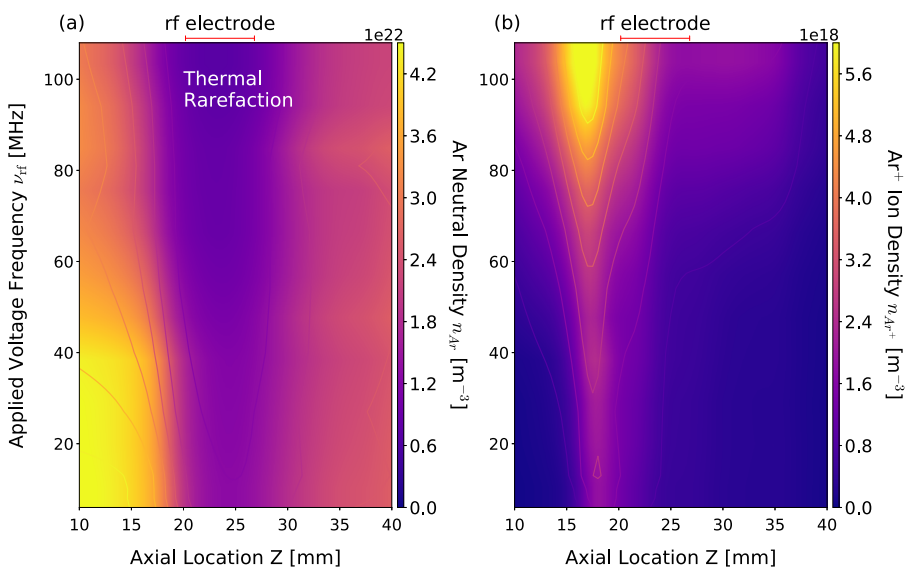
FIG. 3. On-axis phase-averaged (a) neutral argon density n_{Ar} and (b) argon ion density n_{Ar^+} with respect to applied voltage frequency for 6–108 MHz. In (a), the axial location where Ar(3s) density reaches a minimum has been annotated to show the location in Z where thermal rarefaction takes place. Also shown is the location of the rf-powered electrode. Gas flow is in the $+Z$ direction. Applied voltage $\phi_{rf} = 450$ V, 100 sccm argon, plenum pressure 186–226 Pa (1.4–1.8 Torr), wall temperature 325 K.
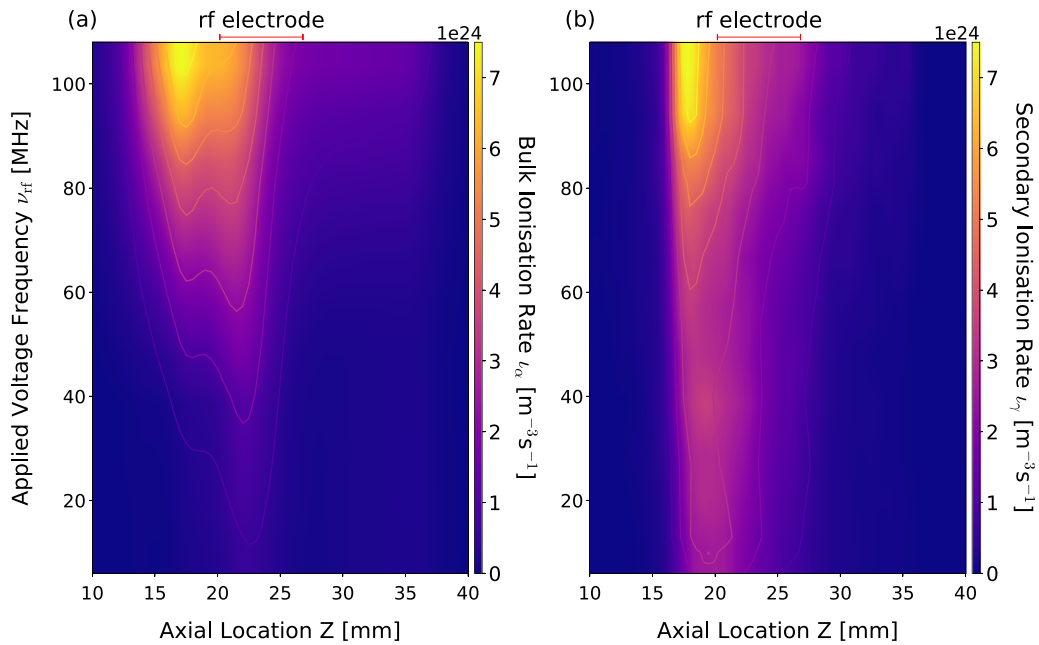
FIG. 4. Phase-averaged secondary electron ionization rate with respect to applied voltage frequency between 6 and 108 MHz. Gas flow is in the $+Z$ direction. Also shown is the location of the rf electrode. Applied voltage $\phi_{rf} = 450$ V, 100 sccm argon, plenum pressure 186–226 Pa (1.4–1.8 Torr), wall temperature 325 K.

upon the wall. Hence, with increasing voltage frequency, secondary electron ionization rates show close agreement with the argon ion density shown previously in Fig. 3(b).

The peak bulk ionization rate in Fig. 4(a) scales proportionally with applied frequency ν_{rf}, while the secondary ionization rate in Fig. 4(b) is of a similar magnitude at 6 MHz as it is at 40.68 MHz. For the bulk electrons driven by the sheath potential this is expected, but for secondaries, an interplay between ionization and gas heating is observed. Increasing the applied voltage frequency from 6 to 13.56 MHz, the maximum rate of secondary ionization decreases by a fifth from 4.4×10^{24} to 3.6×10^{24} m^{-3} s^{-1}. From 13.56–27.12 MHz, the maximum secondary ionization rate decreases more gradually by approximately 14% to 3.1×10^{24} m^{-3} s^{-1}. Here, thermal rarefaction of the neutral gas with increased heating results in a longer electron–neutral mean free path and a reduced secondary electron–neutral collision rate.[42] From 40.68 to 108.48 MHz, the maximum secondary ionization rate correspondingly increases by 50% to 7.6×10^{24} m^{-3} s^{-1} at the axial distance $Z = 18$ mm, corresponding to the upstream end of the dielectric wall. This is consistent with the behavior of the argon ion density at voltage frequencies above 40.68 MHz.

## C. Spatio-temporal electron heating mechanisms with varying single driving frequency

The evolution of the rf phase-resolved electron impact ionization rate with respect to voltage frequency is shown in Fig. 5(a), from 6 to 108.48 MHz at a voltage amplitude of $\phi_{rf} = 450$ V and a location $(R,Z) = (2.1, 21)$ mm, i.e., dielectric wall at the axial center of the powered electrode as shown in Fig. 1. The phase-averaged radial sheath width over this range is shown in Fig. 5(b), as sampled at the axial center of the powered electrode ($Z = 21$ mm).

In Fig. 5(a), three distinct peaks in the rf phase-resolved ionization rate are visible, labeled here as A, B, and C. Peaks A and B represent ionization as a result of bulk electrons heated by sheath collapse and sheath expansion, respectively, i.e., α-mode heating. Peak C represents ionization as a result of γ-mode heating processes, where secondary electrons released from the dielectric wall by ion impact are accelerated to superthermal energies at the phase of full sheath expansion.[35] Peak A lies at phase $\tau \sim 0.2$ when the voltage ϕ_{rf} at the dielectric wall is approaching its most positive value, while peak B lies at $0.4 \leq \tau \leq 0.7$, during which the voltage ϕ_{rf} is decreasing at its fastest rate. Peak C is highest at $\tau = 0.8$, when applied voltage ϕ_{rf} is most negative and the sheath is fully extended. As annotated in Fig. 5(a), there also exists a phase-independent background contribution that increases with the voltage frequency, which occurs due to the presence of the constant dc self-bias potential. In our previous work, this background contribution was found to be associated with peak C, as both bombarding ions and liberated secondaries are accelerated by the self-bias potential, both adding to the γ-mode ionization.[19]

As the applied voltage frequency increases, transitions in the dominant electron heating mechanism are observed in Fig. 5(a). Sheath collapse ionization (peak A) is the dominant ionization mechanism over the range of 6–10 MHz, while remaining visible up to 108.48 MHz. Secondary electron ionization (peak C) dominates over the range 10–27.12 MHz, before saturating into the phase-independent background between 27.12 and 40.68 MHz. Sheath expansion ionization (peak B) increases by a factor of 0.45 over the range 27.12–40.68 MHz before becoming the dominant ionization mechanism at 40.68 MHz and above.

As the voltage frequency ν_{rf} increases from 6 to 108.48 MHz, the rf cycle period decreases from 167 to 9 ns, and the velocity of the sheath edge increases accordingly. Hence, the ionization rate due to
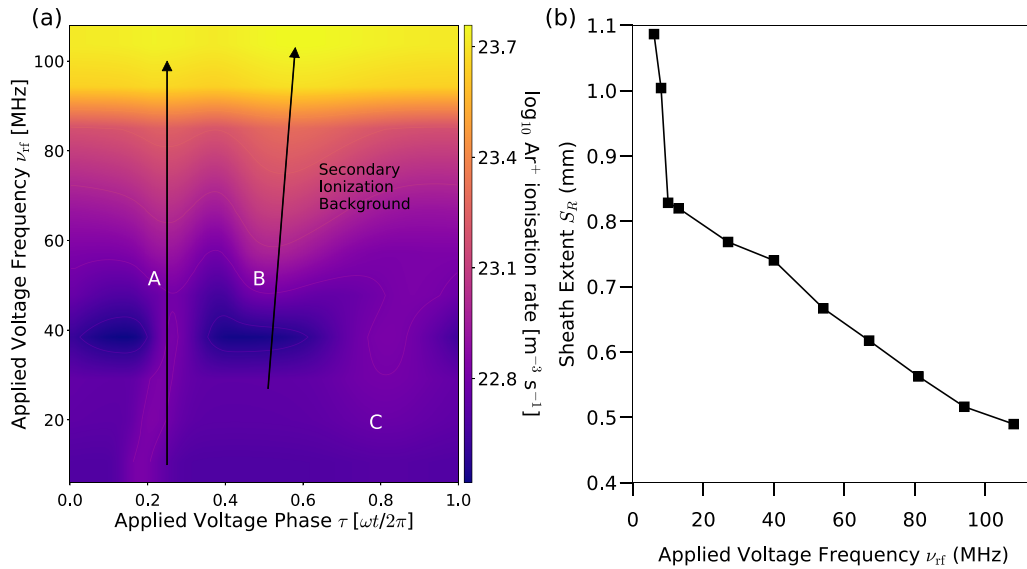
FIG. 5. Simulated (a) argon ionization rates at the dielectric at the axial center of the powered electrode ($Z = 21$ mm) with respect to rf phase τ and (b) phase-averaged sheath extent S_R adjacent to the powered electrode (R, $Z = 2.1$ mm, 21 mm in Fig. 1) with respect to applied voltage frequency $\nu_{\rm rf} = 6$–108 MHz. In (a), peaks A, B, and C represent ionization by sheath collapse, sheath expansion, and accelerated secondary electrons, respectively, their maxima shown by the black arrows. A secondary electron ionization background rate is also indicated. In (b), solid lines have been added to guide the eye. Applied voltage $\phi_{\rm rf} = 450$ V, 100 sccm argon, plenum pressure 186–226 Pa (1.4–1.8 Torr), wall temperature 325 K.

sheath collapse (peak A) and sheath expansion (peak B) heating increase with voltage frequency due to a faster sheath velocity. Secondary electron ionization, represented by peak C in Fig. 5, is observed to increase with voltage frequency over 6.0–13.56 MHz, before it is obscured by a phase-independent background at 40.68 MHz. Over 6.0–10 MHz, peak C increases alongside peak A as a higher overall rate of ionization leads to a higher ion flux on the dielectric wall, generating more secondary electrons. At 40.68 MHz and above, the disappearance of peak C occurs due to a reduction in the absolute time that secondary electrons are accelerated through the sheath, reducing the energy gained and the number of ionisations each secondary electron can induce before cooling into the bulk electron population.

The phase-averaged sheath width S_R, in Fig. 5(b), decreases by a factor of two over the range 6–108.48 MHz, from 1.09 to 0.48 mm. This is consistent with the increase in plasma density shown previously in Fig. 3. The decrease in S_R is steepest over the range 6–10 MHz, where the rate of ionization by secondary electrons increases most rapidly [peak C in Fig. 5(a)]. The phase-independent secondary electron background rate observed at higher voltage frequencies in Fig. 5(a) is likely to result from two possible factors. One is the broadening of peaks A and B with phase, as the absolute time between sheath collapse and expansion decreases. Another is an increase in the argon ion density at higher voltage frequencies due to stronger electron heating during sheath collapse and expansion, leading to a higher (phase-independent) rate of secondary electron emission as the argon ion flux incident on the dielectric radial wall increases.

IV. PLASMA POWER DEPOSITION AND NEUTRAL GAS HEATING

For rf voltages 10–108.48 MHz, it is reasonably to consider that electrons respond instantaneously to oscillations in the sheath potential, while argon ions can be considered to respond only to dc fields. The total rf power deposited into electrons therefore scales in proportion to the applied voltage frequency, as discussed in Sec. III C. In contrast, reducing the applied voltage frequency, while maintaining a constant dc self-bias voltage, increases the proportion of rf power deposited into ions, enhancing the power efficiency of gas heating via ion–neutral charge-exchange collisions.

A. DC self-bias voltage: Effect on ion flux and rf power deposition

Figure 6(a) shows the dc self-bias voltage at the dielectric surface ($R = 2.1$ mm, $Z = 21$ mm, see location 2 in Fig. 2) with respect to the applied voltage frequency in the range 6–108.48 MHz. The associated phase-averaged radial argon ion flux $\Gamma_{\rm Ar+}$ and neutral gas temperature T_g, at the same location are shown in Fig. 6(b), where all simulations were performed with $\phi_{\rm rf} = 450$ V and 100 sccm of argon.

The dc self-bias voltage in Fig. 6(a) exhibits a strong dependence on the applied voltage frequency, increasing by 30% from -212 to -282 V between 6 and 13.56 MHz. Over this range there is a corresponding 10% increase in both the radial ion flux and neutral gas temperature, see Fig. 6(b), from 8.0×10^{20} to 9.0×10^{20} m^{-2} s^{-1}, and 860 to 960 K, respectively. This rapid increase is a result of a higher ion velocity, and enhanced sheath collapse and secondary electron heating [peaks A and C in Fig. 5(a), respectively] both due to a stronger dc self-bias voltage at the radial wall.
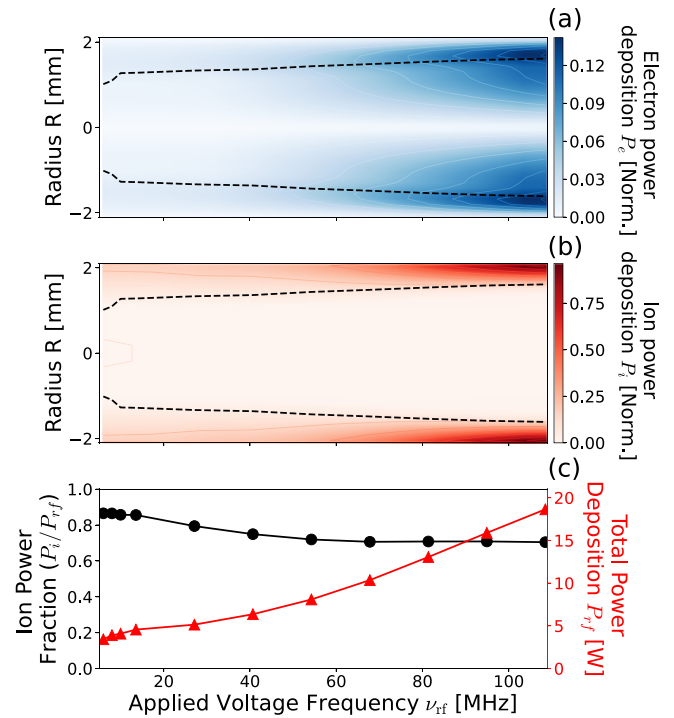
For rf voltage frequencies larger than 13.56 MHz, the dc self-bias voltage varies by less than 7%, decreasing in magnitude with increasing applied voltage frequency. By contrast, from 13.56 to 67.80 MHz, the radial argon ion flux, in Fig. 6(b), continues to increase gradually by a factor of 0.9, from 9.0×10^{20} to 1.7×10^{21} m^{-2} s^{-1}, while the neutral
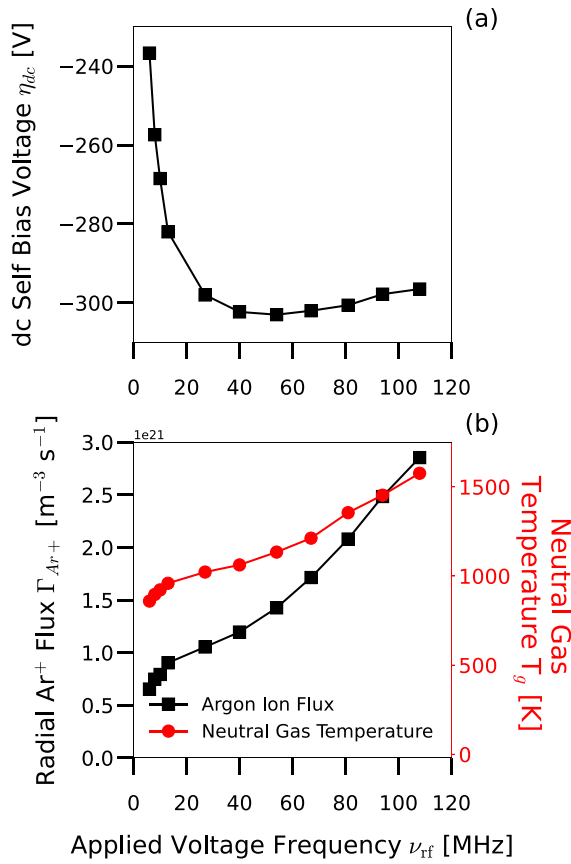
FIG. 6. Phase-averaged (a) dc self-bias voltage at the dielectric radial wall adjacent to the powered electrode (R, $Z = 2.1$ mm, 21 mm in Fig. 1) and (b) the phase-averaged radial argon ion flux Γ_{Ar+} and neutral gas temperature T_g at the same location with respect to the frequency of the applied voltage. Solid lines have been added to guide the eye. Applied voltage $\phi_{rf} = 450$ V, 100 sccm argon, plenum pressure 186–226 Pa (1.4–1.8 Torr), wall temperature 325 K.

FIG. 7. Radially resolved, axially integrated profiles of (a) electron, (b) ion power deposition, and (c) total power deposition, and the ion power fraction, for applied voltage frequencies of 6–108 MHz. Data in panels (a) and (b) are normalized to the total plasma power deposited at 108.48 MHz. The phase-averaged sheath extent at the powered electrode ($Z = 21$ mm) is shown in (a) and (b) by the dashed black line. Solid lines have been added to panel (c) to guide the eye. Applied voltage $\phi_{rf} = 450$ V, 100 sccm argon, plenum pressure 186–226 Pa (1.4–1.8 Torr), wall temperature 325 K.

gas temperature increases by a more modest factor of 0.25, from 960 to 1200 K. The slower increase in gas temperature over this voltage frequency range is attributed to conductive losses to the cold (325 K) dielectric walls and is likely also associated with the increasing thermal rarefaction, resulting in a higher ion–neutral mean free path and consequently and a slower rate of heat transfer to neutrals. From 67.80 to 108.48 MHz, both the radial ion flux and neutral gas temperature increase vary more substantially with respect to voltage frequency, increasing by factors of 1.66 and 1.3, respectively. These trends are consistent with the ionization and ion density trends observed previously in Figs. 3 and 4, and the relatively small change in power deposition limits further increases in the ionization rate and neutral gas heating. This suggests that, while the reduction in sheath extent and increasing thermal rarefaction will increase the average ion velocity, it is likely that the growth in ion flux adjacent to the powered electrode arises due to increased ion densities there, rather than elevated ion velocities, partly due to the small change in dc self-bias voltage over this range.

Figures 7(a) and 7(b) show the steady-state radially resolved, axially integrated rf power deposition into argon ions and

electrons, respectively, with respect to voltage frequency in the range 6–108.48 MHz, employing a constant 450 V discharge with 100 sccm of argon. The volume-integrated total power deposition and fraction of total power deposited into ions is shown in Fig. 7(c) over the same voltage frequency range.

For operation employing voltage frequencies below 40.68 MHz shown in Fig. 7(a), power is predominantly coupled into the electrons close to the radial dielectric wall (i.e., for $R \geq S_R$), with the maximum power deposition observed just within the phase-averaged sheath extent S_R, denoted by the dashed line. Recalling Fig. 5(a), this indicates that the majority of the electron power deposition over this frequency range can be attributed to sheath collapse heating [peak A in Fig. 5(a)], where bulk electrons are accelerated out of the plasma bulk toward the dielectric wall. This agrees with the location of maximum power deposition being found just within the phase-averaged sheath extent, as electrons being accelerated out of the bulk during sheath collapse will experience higher electric fields as the sheath becomes narrower, i.e., as $S_R(t)$ reduces. Secondary electrons, while being the primary ionizing species, represent only 10% of the total electron population, and hence, their dynamics do not significantly influence the electron power deposition. For applied voltage frequencies above 40.68 MHz, the electron power deposition increases both adjacent to the sheath edge and further into the bulk ($R \leq S_R$). This agrees with the increase in sheath

expansion heating [peak B in Fig. 5(a)], in which electrons are accelerated from the sheath toward the central axis. The location of peak electron power deposition remains inside the phase-averaged sheath extent indicating that sheath collapse heating, and to a lesser extent secondary electron acceleration, remain the dominant electron heating mechanisms.

In contrast, Fig. 7(b) shows that ion power deposition occurs solely inside the sheath region ($R \geq S_R$), dictated by the dc self-bias voltage and phase-averaged sheath potential. Notably, the power deposited into ions continues to increase with increasing applied voltage frequency despite the dc self-bias voltage, shown in Fig. 6(a), plateauing at frequencies above 40.68 MHz. This occurs due to the narrowing of the phase-averaged sheath extent with increasing applied voltage frequency, which effectively amplifies the sheath electric field for a fixed dc self-bias voltage, resulting in higher ion acceleration. The increased ion density adjacent to the powered electrode also leads to a larger number of ions undergoing radial acceleration.

The combined effects of Figs. 7(a) and 7(b) are shown in Fig. 7(c), where the total rf power deposition increases with applied voltage frequency, as expected. Between 6 and 13.56 MHz, the total power deposition increases by a factor of 1.3 from 3.4 to 4.6 W, while the ion power fraction remains approximately constant at 86%. Therefore, as the voltage frequency is increased, the corresponding increases in power deposited in the plasma is divided equally between electrons and ions. Over the range 13.56–40.68 MHz, the total power deposition increases by another factor of 1.3 to 6.3 W; however, the ion power fraction reduces to 79%. This indicates that a larger percentage of the additional power is going toward electrons, which can be attributed to the plateauing of the dc self-bias and the continuous decrease in sheath width, shown in Figs. 6(a) and 5(b), respectively. This behavior continues over the range 40.68–108.48 MHz, where the total power deposition increases by a factor of 3 from 6.3 to 18.6 W, and the ion power fraction drops to 70% by 67.80 MHz, beyond which the ion power fraction remains approximately constant.

B. Neutral gas heating efficiency

The relationship between gas heating and rf power deposition with respect to voltage frequency is presented in Fig. 8. Figure 8(a) compares the increase in maximum on-axis neutral gas temperature ΔT and the total power deposition, deposition with respect to voltage frequency for 6–108 MHz at 450 V. Here, ΔT is equal to $T_g - 325$ K, which is the set point for all wall temperatures in the simulation domain. Figure 8(b) shows the gas heating efficiency ($\Delta T/P_{rf}$) with respect to voltage frequency.

Figure 8(a) shows that for 6.0–13.56 MHz, the gas temperature increase ΔT grows by 18%, from 530 to 630 K, while total power deposition increases by 7% from 4.2 to 4.6 W. Over this voltage frequency range in Fig. 8(b), the gas temperature increase per unit power deposited $\Delta T/P_{rf}$ decreases sharply by a factor of 0.1 from 158 to 141 K/W, representing a reduction in the efficiency of gas heating by the plasma. From 13.56 to 67.80 MHz, ΔT increases gradually by a third from 640 to 870 K, while total power deposition increases rapidly by a factor of 2 from 4.5 to 10.3 W. Over this range, the gas temperature increase per unit power deposited decreases by a factor of 0.4 from 141 to 84 K/W, reflecting the aforementioned effects of thermal rarefaction on ion–neutral collisions and the corresponding heating of the neutral gas. From 67.80 to 108.48 MHz, power deposition and gas temperature
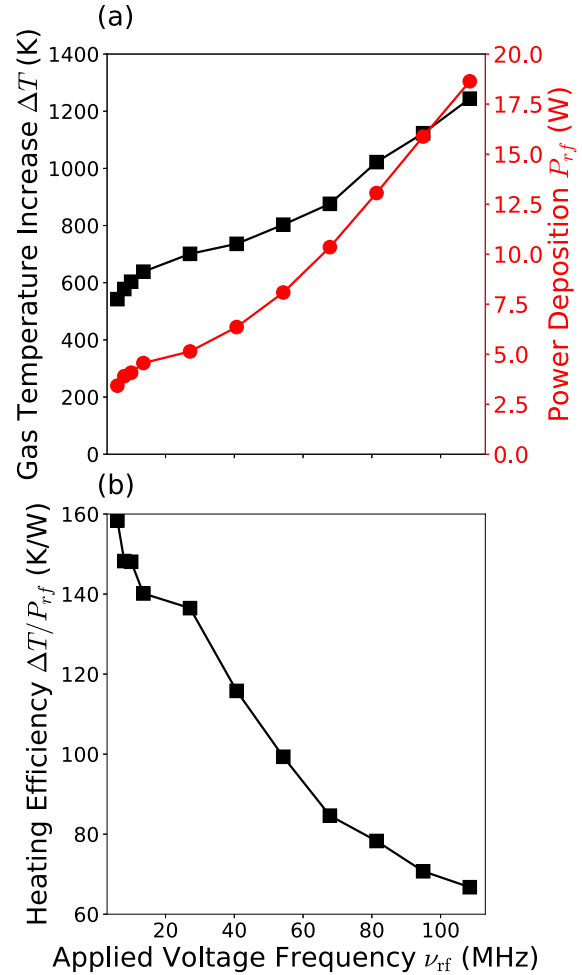

FIG. 8. Phase-averaged values of (a) maximum on-axis ($R = 0$ mm) and (b) neutral gas temperature increase ΔT with respect to total rf power deposition P_{rf}. The applied voltage frequencies for each data point are shown. Solid lines have been added to guide the eye. Applied voltage $\phi_{rf} = 450$ V, 100 sccm argon, plenum pressure 186–226 Pa (1.4–1.8 Torr), wall temperature 325 K.

continue to increase as increased electron heating leads to a higher ion flux, and corresponding increase in secondary electron emission, from the dielectric radial wall, as shown in Fig. 6(b). As further thermal refraction occurs, the temperature increase per unit power is reduced to 67 K/W at 108.48 MHz, less than half of that at 6 MHz. Within the simulated voltage frequency range, it was found that the lowest frequencies produced the highest temperature increase per unit power deposited, up to $\sim$159 K/W at 6 MHz. It is perhaps also useful to consider that the factor ≈ 4 increase in power from 6 MHz to 108.48 MHz is greater than the factor ≈ 2.5 decrease in heating efficiency. As such, if the power were to be held constant across all driving voltage frequencies, the higher frequencies would experience a disproportionately larger drop in power, ion density, ion flux, and hence ion–neutral charge exchange heating as compared to lower frequencies. It can therefore be postulated that the demonstrated trend in heating

efficiency will also be expected when considering a power-specific scenario.

There is a clear indication from Figs. 8(a) and 8(b) that attaining a higher gas temperature beyond 13.56 MHz requires increasingly higher voltage frequencies and hence higher input power, in order for electron heating to sufficiently offset the effects of thermal rarefaction. Hence, there is a trade-off between the maximum obtainable neutral gas temperature and the thermal efficiency of the system. Thermal efficiency is maximized for lower operating frequencies, while the maximum neutral gas temperature increases at higher frequencies in proportion to the applied power. Therefore, a potential avenue to simultaneously increase the neutral gas temperature and the thermal efficiency may be achieved through maximizing the ion power deposition by employing high voltage, low frequency discharges. Although, in these cases, there is also likely to be a trade-off between the maximum obtainable neutral gas temperature and the thermal efficiency of the system.

V. CONCLUSIONS

Two-dimensional fluid-kinetic simulations were performed to study changes in the heating of electrons, ions, and neutrals with varying applied voltage frequency in an rf capacitively coupled plasma microthruster. The discharge was operated in 100 sccm argon at 186–226 Pa (1.4–1.8 Torr) plenum pressure with 325 K walls, under applied voltage frequencies ranging from 6 to 108 MHz at a fixed voltage amplitude of 450 V. Three voltage frequency ranges were investigated, exhibiting distinct changes in the ion and electron power deposition mechanisms: a low-frequency range 6–13.56 MHz, a mid-frequency range 13.56–40.68 MHz, and a high-frequency range 40.68–108.48 MHz. At lower voltage frequencies of 6–13.56 MHz, γ-mode heating is the primary electron heating mechanism and 85% of the rf power is deposited into argon ions for the heating of neutrals via ion–neutral charge exchange. This lower voltage frequency range was found to produce the greatest gas temperature increase per unit of power deposited, and a greater sheath width and volume in which ions accelerate and undergo ion–neutral gas heating. At 13.56–40.68 MHz, a transition of dominant heating mode from γ to α occurs, and only small increases in the argon ion density and gas temperature with respect to voltage frequency were observed. These relatively small increases were explained by the rarefaction of the neutral gas, and a greater fraction of power being transferred by α-mode heating into low-energy bulk electrons, which ionize less efficiently than secondary electrons. Higher voltage frequencies of 40.68–108.48 MHz produced the highest overall gas temperature, power deposition, and argon ion flux due to increased α-mode heating. However, the temperature increase per unit power deposited is less than half of that for the lower frequencies below 13.56 MHz, and only 70% of the rf power is deposited into ions. Developing micropropulsion systems capable of maintaining higher thermal efficiencies, such as those operated in the relatively low frequency regime below 13.56 MHz, is of significant interest to the continued development of microsatellite platforms.

ACKNOWLEDGMENTS

AUTHOR DECLARATIONS
Conflict of Interest

The authors have no conflicts to disclose.

Author Contributions

Sid Leigh: Conceptualization (equal); Data curation (lead); Formal analysis (lead); Investigation (lead); Visualization (lead); Writing – original draft (lead); Writing – review & editing (supporting). **Scott J. Doyle:** Conceptualization (lead); Data curation (supporting); Formal analysis (supporting); Investigation (supporting); Supervision (supporting); Visualization (supporting); Writing – original draft (supporting); Writing – review & editing (lead). **Gregory J. Smith:** Formal analysis (supporting); Investigation (supporting); Writing – original draft (supporting); Writing – review & editing (supporting). **Andrew Robert Gibson:** Formal analysis (supporting); Methodology (supporting); Writing – review & editing (supporting). **R. W. Boswell:** Conceptualization (supporting); Writing – review & editing (supporting). **Christine Charles:** Conceptualization (supporting); Writing – review & editing (supporting). **James Dedrick:** Conceptualization (equal); Formal analysis (equal); Funding acquisition (equal); Investigation (supporting); Project administration (lead); Supervision (lead); Writing – original draft (supporting); Writing – review & editing (equal).

DATA AVAILABILITY

The data that support the findings of this study are available from the corresponding author upon reasonable request.

REFERENCES

[1]R. A. Deepak and R. J. Twiggs, "Thinking out of the box: Space science beyond the CubeSat," J. Small Satell. **1**(1), 3–7 (2012).

[2]D. Scharfe and A. Ketsdever, "A review of high thrust, high delta-V options for microsatellite missions," AIAA Paper No. 209-4824, 2009.

[3]I. Levchenko, K. Bazaka, Y. Ding, Y. Raitses, S. Mazouffre, T. Henning, P. J. Klar, S. Shinohara, J. Schein, L. Garrigues, M. Kim, D. Lev, F. Taccogna, R. W. Boswell, C. Charles, H. Koizumi, Y. Shen, C. Scharlemann, M. Keidar, and S. Xu, "Space micropropulsion systems for Cubesats and small satellites: From proximate targets to furthermost frontiers," Appl. Phys. Rev. **5**(1), 011104 (2018).

[4]Y. Ulybyshev, "Satellite constellation design for complex coverage," J. Spacecr. Rockets **45**(4), 843–849 (2008).

[5]M. Martinez-Sanchez and J. E. Pollard, "Spacecraft electric propulsion—An overview," J. Propul. Power **14**(5), 688–699 (1998).

[6]S. Mazouffre, "Electric propulsion for satellites and spacecraft: Established technologies and novel approaches," Plasma Sources Sci. Technol. **25**(3), 033002 (2016).

[7]D. Rafalskyi and A. Aanesland, "Brief review on plasma propulsion with neutralizer-free systems," Plasma Sources Sci. Technol. **25**(4), 043001 (2016).

[8]A. Dunaevsky, Y. Raitses, and N. J. Fisch, "Plasma acceleration from radio-frequency discharge in dielectric capillary," Appl. Phys. Lett. **88**(25), 251502 (2006).

[9]K. Lemmer, "Propulsion for CubeSats," Acta Astronaut. **134**, 231–243 (2017).

[10]A. Poghosyan and A. Golkar, "CubeSat evolution: Analyzing CubeSat capabilities for conducting science missions," Prog. Aerosp. Sci. **88**, 59–83 (2017).

[11]M. Magarotto, S. Di Fede, N. Souhair, S. Andrews, and F. Ponti, "Numerical suite for cathodeless plasma thrusters," Acta Astronaut. **197**, 126–138 (2022).

[12]J. Zhou, D. Pérez-Grande, P. Fajardo, and E. Ahedo, "Erratum: Numerical treatment of a magnetized electron fluid model within an electromagnetic plasma thruster simulation code (2019 *Plasma Sources Sci. Technol.* **28** 115004)," Plasma Sources Sci. Technol. **29**(1), 019601 (2020).

[13]T. S. Ho, C. Charles, and R. W. Boswell, "Redefinition of the self-bias voltage in a dielectrically shielded thin sheath RF discharge," J. Appl. Phys. **123**(19), 193301 (2018).

[14]D. M. Goebel and I. Katz, *Fundamentals of Electric Propulsion* (Wiley, Hoboken, NJ, 2008).

[15]C. Charles, R. W. Boswell, and K. Takahashi, "Investigation of radiofrequency plasma sources for space travel," Plasma Phys. Controlled Fusion **54**(12), 124021 (2012).

[16]D. Tsifakis, C. Charles, and R. Boswell, "An inductively-coupled plasma electrothermal radiofrequency thruster," Front. Phys. **8**, 34 (2020).

[17]T. Lafleur and C. S. Corr, "Characterization of a radio-frequency inductively coupled electrothermal plasma thruster," J. Appl. Phys. **130**(4), 043304 (2021).

[18]C. Charles and R. W. Boswell, "Measurement and modelling of a radiofrequency micro-thruster," Plasma Sources Sci. Technol. **21**(2), 022002 (2012).

[19]S. J. Doyle, C. Charles, T. S. Ho, R. W. Boswell, A. R. Gibson, P. Tian, J. P. Dedrick, J. Flatt, and M. J. Kushner, "Spatio-temporal plasma heating mechanisms in a radio frequency electrothermal microthruster," Plasma Sources Sci. Technol. **27**(8), 085011 (2018).

[20]W. Liang, C. Charles, L. Raymond, A. Stuchbery, K. Surakitbovorn, L. Gu, R. W. Boswell, and J. Rivas-Davila, "An integrated RF power delivery and plasma micro-thruster system for nano-satellites," Front. Phys. **6**, 115 (2018).

[21]A. D. Greig, C. Charles, N. Paulin, and R. W. Boswell, "Volume and surface propellant heating in an electrothermal radio-frequency plasma micro-thruster," Appl. Phys. Lett. **105**(5), 54102 (2014).

[22]T. S. Ho, C. Charles, and R. W. Boswell, "Neutral gas heating and ion transport in a constricted plasma flow," Phys. Plasmas **24**(8), 84501 (2017).

[23]C. Charles, R. W. Boswell, A. Bish, V. Khayms, and E. F. Scholz, "Direct measurement of axial momentum imparted by an electrothermal radiofrequency plasma micro-thruster," Front. Phys. **4**, 19 (2016).

[24]T. S. Ho, C. Charles, and R. W. Boswell, "A comprehensive cold gas performance study of the pocket rocket radiofrequency electrothermal microthruster," Front. Phys. **4**, 55 (2017).

[25]C. Charles, W. Liang, L. Raymond, J. Rivas-Davila, and R. W. Boswell, "Vacuum testing of a miniaturized switch mode amplifier powering an electrothermal plasma micro-thruster," Front. Phys. **5**, 36 (2017).

[26]M. Manente, F. Trezzolani, M. Magarotto, E. Fantino, A. Selmo, N. Bellomo, E. Toson, and D. Pavarin, "Regulus: A propulsion platform to boost small satellite missions," Acta Astronaut. **157**, 241–249 (2019).

[27]N. Bellomo, M. Magarotto, M. Manente, F. Trezzolani, R. Mantellato, L. Cappellini, D. Paulon, A. Selmo, D. Scalzi, M. Minute, M. Duzzi, A. Barbato, A. Schiavon, S. Di Fede, N. Souhair, P. De Carlo, F. Barato, F. Milza, E. Toson, and D. Pavarin, "Design and in-orbit demonstration of regulus, an iodine electric propulsion system," CEAS Space J. **14**, 79–90 (2022).

[28]A. D. Greig, C. Charles, and R. W. Boswell, "Spatiotemporal study of gas heating mechanisms in a radio-frequency electrothermal plasma micro-thruster," Front. Phys. **3**, 84 (2015).

[29]B. G. Heil, U. Czarnetzki, R. P. Brinkmann, and T. Mussenbrock, "On the possibility of making a geometrically symmetric RF-CCP discharge electrically asymmetric," J. Phys. D **41**(16), 165202 (2008).

[30]C. Charles, R. Hawkins, and R. W. Boswell, "Particle in cell simulation of a radiofrequency plasma jet expanding in vacuum," Appl. Phys. Lett. **106**(9), 093502 (2015).

[31]H. D. Hagstrum, "Theory of auger ejection of electrons from metals by ions," Phys. Rev. **96**(2), 336–365 (1954).

[32]T. A. Lafleur, R. W. Boswell, and J.-P. Booth, "Enhanced sheath heating in capacitively coupled discharges due to non-sinusoidal voltage waveforms," Appl. Phys. Lett. **100**(19), 194101 (2012).

[33]A. Derzsi, I. Korolov, E. Schüngel, Z. Donkó, and V. Schulz–von der Gathen, "Effects of fast atoms and energy-dependent secondary electron emission yields in PIC/MCC simulations of capacitively coupled plasmas," Plasma Sources Sci. Technol. **24**(3), 34002 (2015).

[34]K. H. Schoenbach, A. El-Habachi, W. Shi, and M. Ciocca, "High-pressure hollow cathode discharges," Plasma Sources Sci. Technol. **6**(4), 468–477 (1997).

[35]A. V. Phelps and Z. L. Petrovic, "Cold-cathode discharges and breakdown in argon: Surface and gas phase production of secondary electrons," Plasma Sources Sci. Technol. **8**(3), R21–R44 (1999).

[36]M. A. Lieberman and A. J. Lichtenberg, *Principles of Plasma Discharges and Materials Processing*, 2 ed. (Wiley, New Jersey, 2005).

[37]J. J. Shi and M. G. Kong, "Evolution of discharge structure in capacitive radiofrequency atmospheric microplasmas," Phys. Rev. Lett. **96**(10), 105009 (2006).

[38]J. Schulze, B. G. Heil, D. Luggenhölscher, R. P. Brinkmann, and U. Czarnetzki, "Stochastic heating in asymmetric capacitively coupled RF discharges," J. Phys. D **41**(19), 195212 (2008).

[39]J. Schulze, Z. Donkó, D. Luggenhölscher, and U. Czarnetzki, "Different modes of electron heating in dual-frequency capacitively coupled radio frequency discharges," Plasma Sources Sci. Technol. **18**(3), 34011 (2009).

[40]V. Schulz-von der Gathen, A. Derzsi, K. Dittmann, T. Hemke, J. Meichsner, and Z. Donkó, "Ionization by drift and ambipolar electric fields in electronegative capacitive radio frequency plasmas," Phys. Rev. Lett. **107**(27), 275001 (2011).

[41]A. D. Greig, C. Charles, and R. W. Boswell, "Simulation of main plasma parameters of a cylindrical asymmetric capacitively coupled plasma micro-thruster using computational fluid dynamics," Front. Phys. **2**, 80 (2015).

[42]S. J. Doyle, A. R. Gibson, R. W. Boswell, C. Charles, and J. P. Dedrick, "Inducing locally structured ion energy distributions in intermediate-pressure plasmas," Phys. Plasmas **26**(7), 073519 (2019).

[43]N. Schmidt, J. Schulze, E. Schüngel, and U. Czarnetzki, "Effect of structured electrodes on heating and plasma uniformity in capacitive discharges," J. Phys. D **46**(50), 505202 (2013).

[44]S. J. Doyle, T. A. Lafleur, A. R. Gibson, P. Tian, M. J. Kushner, and J. P. Dedrick, "Enhanced control of the ionization rate in radio-frequency plasmas with structured electrodes via tailored voltage waveforms," Plasma Sources Sci. Technol. **26**(12), 125005 (2017).

[45]L. Wang, P. Hartmann, Z. Donkó, Y.-H. Song, and J. Schulze, "Effects of structured electrodes on electron power absorption and plasma uniformity in capacitive RF discharges," J. Vac. Sci. Technol., A **39**(6), 063004 (2021).

[46]Y. Liu, M. Vass, G. Hübner, D. Schulenberg, T. Hemke, L. Bischoff, S. Chur, D. Steuer, J. Golda, M. Böke, J. Schulze, I. Korolov, and T. Mussenbrock, "Local enhancement of electron heating and neutral species generation in radiofrequency micro-atmospheric pressure plasma jets: The effects of structured electrode topologies," Plasma Sources Sci. Technol. **32**(2), 025012 (2023).

[47]M. A. Lieberman, J. P. Booth, P. Chabert, J. M. Rax, and M. M. Turner, "Standing wave and skin effects in large-area, high-frequency capacitive discharges," Plasma Sources Sci. Technol. **11**(3), 283 (2002).

[48]A. Perret, P. Chabert, J.-P. Booth, J. Jolly, J. Guillon, and P. Auvray, "Ion flux nonuniformities in large-area high-frequency capacitive discharges," Appl. Phys. Lett. **83**(2), 243–245 (2003).

[49]J. Park, I. Henins, H. W. Herrmann, G. S. Selwyn, and R. F. Hicks, "Discharge phenomena of an atmospheric pressure radio-frequency capacitive plasma source," J. Appl. Phys. **89**(1), 20–28 (2001).

[50]D. W. Liu, J. J. Shi, and M. G. Kong, "Electron trapping in radio-frequency atmospheric-pressure glow discharges," Appl. Phys. Lett. **90**(4), 041502 (2007).

[51]S. Y. Moon, D. B. Kim, B. Gweon, and W. Choe, "Driving frequency effects on the characteristics of atmospheric pressure capacitive helium discharge," Appl. Phys. Lett. **93**(22), 221506 (2008).

[52]J. Park, I. Henins, H. W. Herrmann, and G. S. Selwyn, "Gas breakdown in an atmospheric pressure radio-frequency capacitive plasma source," J. Appl. Phys. **89**(1), 15–19 (2001).

[53]A. Perret, P. Chabert, J. Jolly, and J.-P. Booth, "Ion energy uniformity in high-frequency capacitive discharges," Appl. Phys. Lett. **86**(2), 021501 (2005).

[54]S. J. Doyle, A. R. Gibson, R. W. Boswell, C. Charles, and J. P. Dedrick, "Decoupling ion energy and flux in intermediate pressure capacitively coupled plasmas via tailored voltage waveforms," Plasma Sources Sci. Technol. **29**(12), 124002 (2020).

[55]T. S. Ho, C. Charles, and R. W. Boswell, "Performance modelling of plasma microthruster nozzles in vacuum," J. Appl. Phys. **123**(17), 173301 (2018).

[56]A. D. Greig, "Pocket rocket: An electrothermal plasma micro-thruster," Ph.D. thesis (Australian National University, 2015).

08 May 2024 08:45:18

[57]M. J. Kushner, "Hybrid modelling of low temperature plasmas for fundamental investigations and equipment design," J. Phys. D **42**(19), 194013 (2009).

[58]S. J. Doyle, A. R. Gibson, R. W. Boswell, C. Charles, and J. P. Dedrick, "Control of electron, ion and neutral heating in a radio-frequency electrothermal micro-thruster via dual-frequency voltage waveforms," Plasma Sources Sci. Technol. **28**(3), 035019 (2019).

[59]A. Salabaş and R. Peter Brinkmann, "Non-neutral/quasi-neutral plasma edge definition for discharge models: A numerical example for dual frequency hydrogen capacitively coupled plasmas," Jpn. J. Appl. Phys., Part 1 **45**(6R), 5203–5206 (2006).

[60]D. L. Scharfetter and H. K. Gummel, "Large-signal analysis of a silicon read diode oscillator," IEEE Trans. Electron Devices **12**(1), 64–77 (1969).

[61]S. H. Song and M. J. Kushner, "Control of electron energy distributions and plasma characteristics of dual frequency, pulsed capacitively coupled plasmas sustained in Ar and Ar/CF_4/O_2," Plasma Sources Sci. Technol. **21**(5), 055028 (2012).

[62]M. Furman and M. Pivi, "Probabilistic model for the simulation of secondary electron emission," Phys. Rev. Spec. Top.-Accel. Beams **5**(12), 124404 (2002).

[63]P. Tian and M. J. Kushner, "Controlling VUV photon fluxes in low-pressure inductively coupled plasmas," Plasma Sources Sci. Technol. **24**(3), 34017 (2015).

[64]I. Hayashi, Report No. IPPJ-AM-19 (Nagoya Institute of Technology, 1991).

[65]K. Tachibana, "Excitation of the 1s5, 1s4, 1s3, and 1s2 level of argon by low-energy electrons," Phys. Rev. A **34**(2), 1007–1015 (1986).

[66]D. Rapp and P. Englander–Golden, "Total cross sections for ionization and attachment in gases by electron impact. I. Positive ionization," J. Chem. Phys. **43**(5), 1464–1479 (1965).

[67]N. A. Dyatko, Y. Z. Ionikh, I. V. Kochetov, D. L. Marinov, A. V. Meshchanov, A. P. Napartovich, F. B. Petrov, and S. A. Starostin, "Experimental and theoretical study of the transition between diffuse and contracted forms of the glow discharge in argon," J. Phys. D **41**(5), 55204 (2008).

[68]H. W. Ellis, P. Y. Pai, E. W. McDaniel, E. A. Mason, and L. A. Viehland, "Transport properties of gaseous ions over a wide energy range," At. Data Nucl. Data Tables **17**(3), 178–210 (1976).

[69]A. J. Lofthouse, L. C. Scalabrin, and I. D. Boyd, "Velocity slip and temperature jump in hypersonic aerothermodynamics," J. Thermophys. Heat Transfer **22**(1), 38–49 (2008).

[70]Y.-X. Liu, Y.-R. Zhang, A. Bogaerts, and Y.-N. Wang, "Electromagnetic effects in high-frequency large-area capacitive discharges: A review," J. Vac. Sci. Technol., A **33**(2), 020801 (2015).

[71]V. I. Kolobov and D. J. Economou, "The anomalous skin effect in gas discharge plasmas," Plasma Sources Sci. Technol. **6**(2), R1 (1997).

08 May 2024 08:45:18